CrN–NbN nanolayered coatings for enhanced accident tolerant fuels in BWR

Andrea Fazi [a,*], Mohammad Sattari [a], Michal Strach [b], Torben Boll [c,d,e], Krystyna Stiller [a], Hans-Olof Andrén [a], Denise Adorno Lopes [f], Mattias Thuvander [a]

[a] *Department of Physics, Chalmers University of Technology, SE-412 96 Gothenburg, Sweden*
[b] *Chalmers Materials Analysis Laboratory, Chalmers University of Technology, SE-412 96 Gothenburg, Sweden*
[c] *Karlsruhe Institute of Technology (KIT), Institute for Applied Materials – Materials Science and Engineering (IAM-WK), Engelbert-Arnold-Str. 4, 76131 Karlsruhe, Germany*
[d] *Karlsruhe Institute of Technology (KIT), Institute of Nanotechnology (INT), Hermann-von-Helmholtz-Platz 1, 76344 Eggenstein-Leopoldshafen, Germany*
[e] *Karlsruhe Institute of Technology (KIT), Karlsruhe Nano Micro Facility (KNMFi), Hermann-von-Helmholtz-Platz 1, 76344 Eggenstein-Leopoldshafen, Germany*
[f] *Westinghouse Electric Sweden AB, SE-721 63 Västerås, Sweden*

A R T I C L E   I N F O

A B S T R A C T

The accident tolerant fuel (ATF) concept has emerged in the years after the 2011 Fukushima accident as part of a renewed effort in research for light water reactors. The primary focus is to further improve safety measures under and beyond design basis accident conditions, and to improve fuel cladding performance in normal operation. The application of a coating on zirconium claddings can achieve both these aims without extensive changes to the reactor design. Metallic chromium coatings have been profusely studied as solution for pressurized water reactors, but the search for an effective ATF coating able to withstand the environment inside boiling water reactors (BWRs) is still ongoing. In this work, two different versions of a novel nitride coating composition were studied. Zirconium claddings coated with 8 μm thick layers of superlattice CrN–NbN and a nanolayered CrN–NbN were tested in autoclave under BWR operating conditions for 60 days. Scanning electron microscopy, transmission electron microscopy, energy dispersive x-ray spectroscopy, electron back-scattered diffraction, x-ray diffraction, and atom probe tomography were employed to characterize as-deposited and autoclaved samples of these two materials. During exposure, both coating versions formed a stable, dense and passivating oxide scale (200–300 nm thick) on the surface, demonstrating improved oxidation protection under operating conditions. Some differences in the oxide growth mechanism were observed between the superlattice and the nanolayered CrN–NbN coatings, which allowed to glimpse at the effect of the layer thickness on the oxidation protection provided by these coatings. The nano-structured morphology of both coatings remained unaffected by the autoclave test, but a 35 nm thick Zr-Cr-N phase was found at the coating-substrate interface of the superlattice CrN–NbN coated cladding.

1. Introduction

The development of new materials for light water reactors (LWRs) has acquired significant momentum in the years after the nuclear accident that occurred in Fukushima in 2011. These new materials are referred to as accident tolerant fuels (ATFs) or enhanced accident tolerant fuels (EATFs) and promise to increase safety margins in case of a severe accident while improving the fuel performance during normal operation. Research in ATFs can be divided into the search for advanced

fuel cladding tubes and improved fuel pellets. Fuel claddings are traditionally produced from Zr-alloys. Zr has a very low cross-section for thermal neutrons, which was the reason why it was selected for nuclear applications, but it starts reacting exothermally with steam at temperatures above 900 °C. During a severe nuclear accident such temperatures can be reached, and the Zr alloy can start oxidizing, producing hydrogen gas. The oxidation of the cladding can severely affect its mechanical properties and lead to embrittlement and rupture of the tube. The produced hydrogen gas can leak outside the reactor pressure vessel, mix

---

* Corresponding author.
E-mail address: fazi@chalmers.se (A. Fazi).

with air and cause explosions. Impeding the reaction between Zr and steam is at the core of the ATF concept. Two main approaches have been undertaken in order to achieve this goal: integral substitution of the Zr-alloys as cladding material (long-term solution), and the application of a protective coating on the outer surface of a conventional Zr-cladding (short-term solution). The second approach is considered a good intermediate step because it allows to accomplish the principal ATF objective without the need for an extensive redesign and licensing of the reactors currently in operation [1–5].

Cr coatings have emerged in recent years as the main candidate ATF coatings for pressurized water reactors (PWRs) [6], but have had little success in the far more oxidizing BWR environment. Nitride coatings are well known as hard coatings for cutting tools, drill bits and other applications where extreme resistance to abrasion, mechanical strength, corrosion resistance and thermal stability are a necessity. These coatings can be deposited with physical vapor deposition (PVD) or chemical vapor deposition. PVD has the advantage of a lower process temperature, controllable coating composition and a tunable coating structure [7]. CrN and TiN are among the most commonly utilized nitride coatings [8]. TiN has outstanding mechanical properties, but it tends to oxidize quickly when exposed to temperatures above 500 °C. CrN, on the other hand, is able to form a dense layer of chromia and shows better oxidation resistance [9]. Both coatings were taken into consideration as potential ATF coatings but were unable to survive boiling water reactor (BWR) operating conditions [10]. CrN in particular, being a chromia forming coating, was found to dissolve into the cooling water, as this oxide is not stable in the water chemistry of a BWR [11–14]. For the same reason, metallic Cr coatings, despite being very promising for PWR environments, cannot form the passivating chromia layer necessary to survive in BWR environment. NbN is rarely employed as a monolithic coating, but it has been studied as component of multilayer coatings together with CrN or TiN for its positive effects on chemical stability, corrosion resistance and wear rates [15–19]. To obtain a multilayer coating, two targets of different metals are positioned opposite to each other inside the deposition chamber. During deposition both targets will be active, and layers will be formed by rotating the substrate towards one target at the time. By controlling the rotation speed it is possible to control the thickness of the layers down to the nanometer scale [9,15,16,20,21]. Layered and superlattice nitride coatings have been shown to perform well in simulated accident scenarios [22–25] and are promising candidates for ATFs. Cr-Nb metallic alloys have also been studied as ATF coatings and have exhibited improved corrosion and wear resistance compared to pure Cr [26] further demonstrating the potential of Nb additions to chromia forming systems.

In this work, cladding tubes made from the commercial HiFi™ Zr alloy, coated with two different versions of nanolayered CrN–NbN coatings, were tested in BWR water chemistry. Scanning electron microscopy (SEM), energy dispersive x-ray spectroscopy (EDS), transmission electron microscopy (TEM), scanning TEM (STEM), STEM-EDS, electron energy loss spectroscopy (EELS), x-ray diffraction (XRD), and atom probe tomography (APT) were used to characterize the coated cladding before and after autoclave exposure. The objective of the study was to test the corrosion resistance of the coatings, and to understand the role of Nb and of the nanolayered morphology in the formation of stable Cr-rich oxides under BWR operating conditions. Finding a nitride coating able to provide enhanced resistance to high temperature corrosion in steam and elevated hardness, would represent an important step forward in the development of ATF for BWRs. Debris fretting is currently one of the principal causes of fuel rod failure in BWRs [27–29]. Fuel rod failure due to debris fretting requires the operator to stop the reactor and exchange the damaged fuel assembly. Hard coatings could remedy this problem, offering one additional reason for the implementation of ATFs.

2. Materials and methods

An 8 μm thick CrN–NbN coating was deposited onto a zirconium cladding substrate with PVD. Two versions of this coating were analyzed in this work: superlattice (SL) CrN–NbN from Ionbond – IHI Group, and nanolayered (NL) CrN–NbN from TEER Coatings Ltd. Both versions were deposited with magnetron sputtering PVD (MS-PVD). The deposition temperature was set to never exceed 400 °C so to avoid inducing any undesired change in the cladding microstructure. Plasma cleaning of the uncoated substrate tubes was performed before starting the deposition in order to prepare the surface and guarantee better coating adhesion. The SL CrN–NbN presents alternating layers of CrN and NbN which have equal thicknesses of 2 nm (periodicity of 4 nm). In the case of the NL CrN–NbN the layer thickness ranges between 5 nm and 10 nm. Both coatings were designed to have an average Cr:Nb ratio of 2:1 (at.%). The coatings were deposited on Zr cladding tubes made of the HiFi™ alloy (1.50 wt.% Sn, 0.40 wt.% Fe, 0.10 wt.% Cr, 0.08 wt.% Ni, and balance Zr [30]). The as-deposited claddings were cut into 4 cm long portions. Some of the obtained samples were kept as-deposited, while other samples were exposed to autoclave corrosion testing in BWR water chemistry for a total duration of 60 days. The autoclave corrosion test was performed in collaboration with Toshiba Energy Systems & Solutions Corporation for 60 days at 300 °C, 10 MPa and 8.3 ppm of dissolved oxygen (conditions representing the top of a fuel rod in a BWR). The autoclave corrosion test was performed in a closed loop setup. After flowing through the pressure vessel, the water was circulated through a control tank and ion exchange resin cylinders in order to maintain the concentration of oxygen constant at the set value and to remove any dissolved ionic species. Afterwards, a low-speed saw was used to cut both as-deposited and autoclaved samples into rings (5–20 mm in height) that were subsequently cut in half along the axial direction. To access the outer surface of the coated claddings, the half-rings were mounted onto SEM-compatible aluminum stubs (coated surface pointing upward). To access the cross-section of the tubes, the half-rings were mounted in conductive Bakelite, then ground and polished with SiC paper and diamond suspensions. A focused ion beam/scanning electron microscopy dual-beam FEI Versa 3D workstation was used to prepare both TEM and APT specimens implementing well-known lift-out procedures [31–33]. All FIB/SEM sample preparation was performed at room temperature and no cryo-FIB/SEM sample preparation was involved. It has been reported in literature that room temperature FIB milling can promote the formation of hydrides in Zr-alloys [34]. The effect on solute elements was demonstrated to be minimal [34] and was deemed not to be detrimental for the scope of this work which focuses mainly on the oxidation and transformation of the nitride coatings. TEM specimens were mounted on Cu half-grids, while APT specimens were mounted and sharpened on premade Si-posts disposed onto a coupon compatible with the CAMECA LEAP 4000X HR instrument. SEM and SEM-EDS were performed on a JEOL 7800F Prime SEM equipped with an X-Max^N EDS detector from Oxford Instruments. TEM imaging was performed on an FEI Tecnai T20 LaB6, while STEM images, and STEM-EDS and EELS analysis were collected on an FEI Titan 80–300. XRD analysis was carried out on a Bruker D8 Discover with a Cu source, and an Eiger 2R 500 K 2D detector. Sample positioning and scan parameters were optimized for each sample. NL CrN–NbN coated samples were measured for 12 h each, with a 0.02 degree step size, variable slit and 1D detector setting. As-deposited SL CrN–NbN was measured for 10 h using a fixed slit, 0.02 degree step size and 1D detector setting. Autoclave exposed SL CrN–NbN was measured for 3 h using a variable slit and 1D detector setting. Data was processed using Bruker Eva software. All electron microscopy-based investigations, XRD analysis, and specimen preparation were performed at Chalmers Materials Analysis Laboratory (CMAL). The APT specimens were run at Karlsruhe Nano Micro Facility (KNMFi) at the Karlsruhe Institute of Technology (Karlsruhe, Germany) in a CAMECA LEAP 4000X HR. All samples were run in laser mode with 200 kHz laser pulse frequency, at 40 K specimen

temperature, 70 pJ laser pulse energy and 0.2–0.5% evaporation rate. CAMECA IVAS 3.6.14 software was used for data evaluation and reconstruction.

3. Results

An overview of the outer surface and cross-section of as-deposited and autoclave exposed coatings is presented in Fig. 1(a). In these SEM images both as-deposited coatings appear fully dense, and no porosity is visible, neither in the bulk of the coating nor at the interface with the substrate. The SL coating appears fully homogeneous with no change in color throughout the thickness of the coating. In the case of the NL coating, instead, the lower third of the coating (closer to the substrate) presents a darker contrast, while the top part of the coating is slightly lighter in color. This is likely due to a larger presence of Nb in the top layer of the coating, as confirmed by the SEM-EDS map of the same area presented in Fig. 1(b). The outer surfaces of the coatings are presented in top view, and they display the typical morphology of MS-PVD coatings. Here the top of the columnar grains can be distinguished. Some horizontal trenches can be seen on the outer surface. These are probably due to scratches present on the HiFi™ cladding surface.

After exposure, an oxide scale of a few hundred nanometer was found on both coatings. These oxide scales show acicular, elongated crystals on the outer surface. SEM-EDS chemical analysis of the oxides on both coatings was performed by mapping a large area of the outer surface of the exposed coatings. The obtained composition for the as-deposited and exposed coatings is presented in Table 1. In the as-deposited coating, the N concentration is measured to around 50 at.%,

and Cr and Nb represent the remaining 50 at.%.

The ratio between Cr and Nb is reasonably close to the targeted 2:1, but it is worth mentioning that excess Cr can be measured in both coatings. The composition obtained from the exposed outer surfaces is also very similar for both the SL and NL coatings: about 52–53 at.% O, 25–27 at.% Cr, 11–12 at.% Nb, and 5–7 at.% N. The N signal could either originate from the coating underneath the oxide scale due to the interaction volume with the e-beam being larger than the oxide thickness or, more probably, represent the incomplete oxidation of the coating with some remaining N in the form of residual oxynitride grains. Impurities of Ni and Al could also be found in the oxide but are not present in the as-deposited coatings. These impurities must originate from the autoclave environment (sample holders and autoclave walls).

TEM was used to access the nanolayered morphology of the coatings and better study the oxides. Fig. 2 shows a series of BF-TEM images collected on the cross-sectional lamellae prepared from SL CrN–NbN coating before and after exposure in autoclave. The SL coating presents layers with a periodicity in the range of 4–5 nm. On top of this layered morphology, darker and brighter regions can be found. These changes in contrast could be associated with defect density and chemical inhomogeneities, and can be found both in the as-deposited and the exposed sample. On the outer surface of the exposed SL sample a 200–300 nm thick oxide scale is found. This oxide is subdivided into a layered inner oxide and an outer oxide characterized by the presence of elongated crystals.

The oxide-coating interface appears jagged, and the oxidation front penetrates deeper in certain regions of the SL coating. The superlattice structure is not lost after the exposure, and the 2–3 nm thick individual
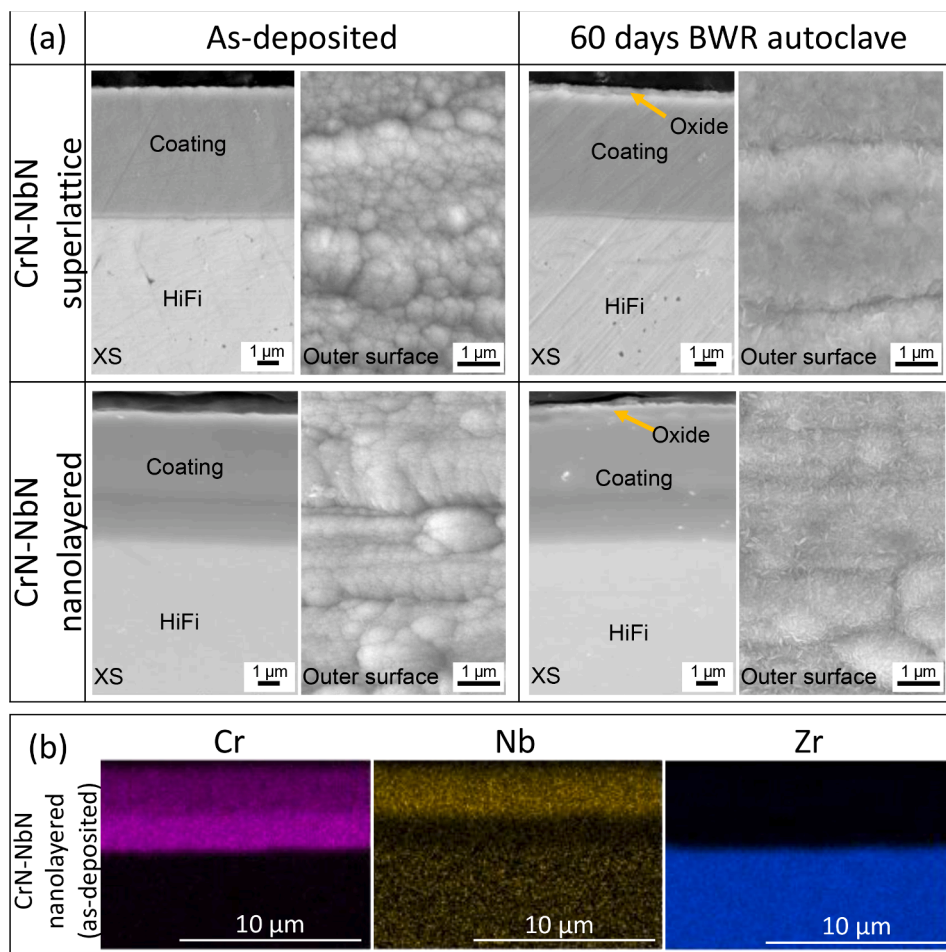

Fig. 1. (a) SEM images of superlattice and nanolayered CrN–NbN coatings before and after autoclave exposure. Both cross-sectional view and top view are presented. (b) SEM-EDS map on cross-section of as-deposited nanolayered CrN–NbN.

Table 1

Chemical composition of the coatings measured with EDS from the outer surface of the coated claddings. Measurements performed using an acceleration voltage of 12 kV.

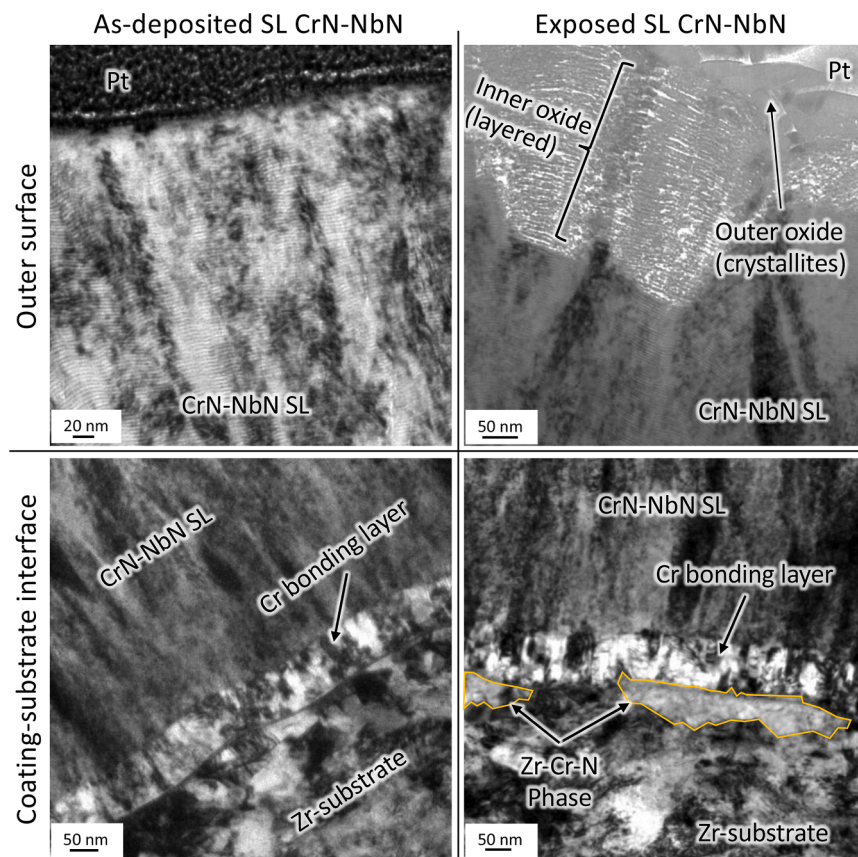|	Cr (at.%)	error (±at.%)	Nb (at.%)	error (±at.%)	N (at.%)	error (±at.%)	O (at.%)	error (±at.%)	Ni (at.%)	error (±at.%)	Al (at.%)	error (±at.%)
as-dep SL CrN–NbN	**37.0**	0.1	**15.6**	0.1	**47.4**	0.2	–	–	–	–	–	–
expos. SL CrN–NbN	**24.8**	0.1	**10.7**	0.1	**6.8**	0.3	**52.1**	0.3	**4.3**	0.1	**1.3**	0.1
as-dep NL CrN–NbN	**32.2**	0.1	**14.3**	0.1	**53.6**	0.2	–	–	–	–	–	–
expos. NL CrN–NbN	**27.0**	0.1	**12.5**	0.1	**4.6**	0.2	**52.8**	0.2	**3.1**	0.1	–	–

Fig. 2. BF-TEM images of superlattice CrN–NbN coating. Both outer surface (top row) and coating-substrate interface (bottom row) are presented in the as-deposited condition (left column) and after autoclave exposure (right column).

layers are still visible and distinguishable. The layered morphology is conserved in the inner layered oxide that is visible in the BF-TEM image. From BF-TEM it is difficult to tell if these layers in the oxide are due to different density (for example pores) or if it is linked to different chemical compositions. Moving away from the outer surface down to the coating-substrate interface, a 50–60 nm thick Cr bonding layer can be found. This layer has a homogeneous thickness across the interface and it has sharp interfaces with both the Zr substrate and the SL CrN–NbN coating. After exposure to autoclave, the interfacial area has undergone some small changes. The interface between the Cr bonding layer and the SL CrN–NbN coating appears less sharp and more jagged, while a new phase is found nucleating at the interface between the Cr bonding layer and the Zr substrate. This phase was identified as a Zr-Cr-N phase thanks to APT (see APT results presented below). It seems to grow inward, in the direction of the Zr substrate, and it forms a discontinuous layer at the interface.

BF-TEM images of the NL CrN–NbN coating before and after autoclave exposure are presented in Fig. 3. Here it is clear that the periodicity of the layers is very different between the SL and the NL coatings. The NL CrN–NbN coating presents alternating layers with a periodicity around 10 nm, and the different layers (bright and dark) have different

thicknesses. The layered morphology is conserved after the exposure and appears mostly unchanged. Well-defined columnar grains (50–100 nm wide) are visible in both the as-deposited and exposed samples and stretch across the entire micrograph. After exposure, a 200–250 nm thick oxide scale is found on the outer surface of the coating. This scale is characterized by a denser outer layer with larger crystallites and a layered, less dense, inner band that seems to have conserved the original layered morphology of the coating.

The inner, layered oxide developed on the NL CrN–NbN coating presents less porosities and defects when compared with the inner oxide developed on the SL coating. The oxide-coating interface is relatively flat, but small bits of unoxidized coating layers can be sometime found protruding into the inner oxide, as highlighted by the arrows in Fig. 3. The outer oxide presents relatively large grains with crystallites around 50 nm in size and a homogenous thickness throughout the exposed cross-section. The NL CrN–NbN coating also contains a Cr bonding layer, but this time it is significantly thicker (200–250 nm). No change can be seen at the interface of the NL coating before and after exposure. Higher magnification BF-TEM micrographs of the oxide scale developed during the autoclave exposure on the outer surface of the NL CrN–NbN coated cladding are presented in Fig. 4. Selected area diffraction patterns
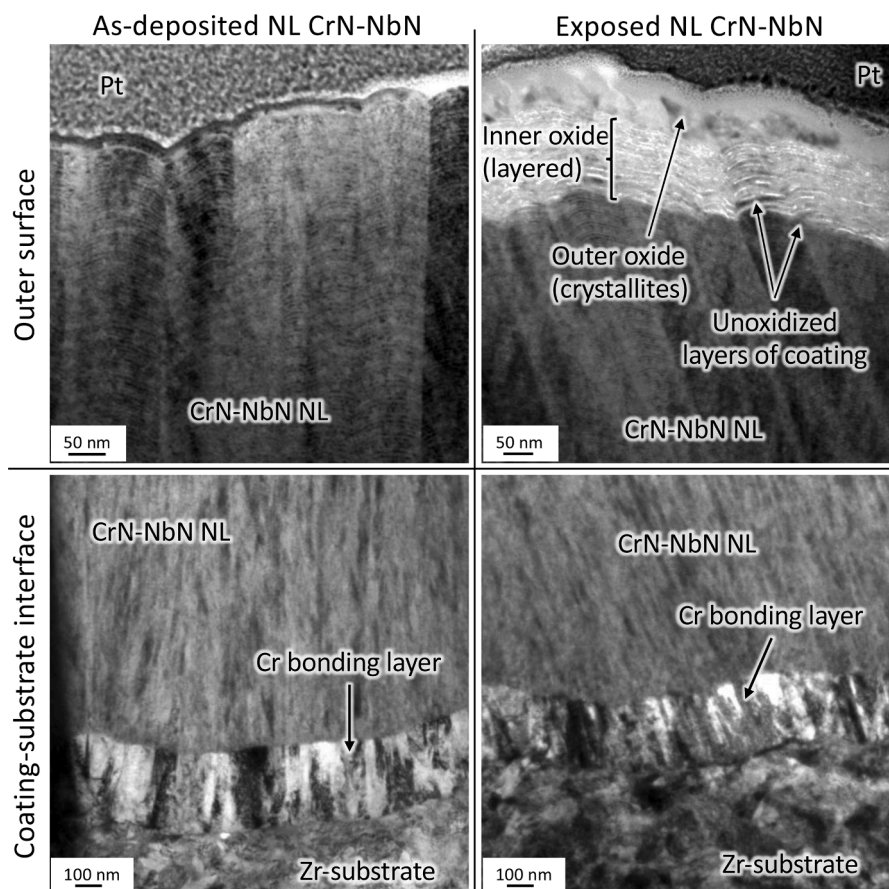
Fig. 3. BF-TEM images of nanolayered CrN–NbN coating. Both outer surface (top row) and coating-substrate interface (bottom row) are presented in the as-deposited condition (left column) and after autoclave exposure (right column).

(SADPs) of the outer, larger crystallites were collected and indexed. This phase was identified as tetragonal $NbCrO_4$. Box A presented in Fig. 5 shows a lower magnification BF-TEM image where it is possible to see the columnar grains stretching for $1–2$ μm from top to bottom. In Box B of the same figure the region of transition from high Nb content to low Nb content (top 2/3rd of the coating vs lower 1/3rd of the coating) is presented. Around this area the grain structure of the coating changes and much smaller grains appear.

STEM images and STEM-EDS mapping of the oxides developed after autoclave on the outer surface of the SL and NL CrN–NbN coatings are presented in Fig. 6. First, it is interesting to notice that the crystallites of the outer oxide seem to be on average larger in the NL coating than in the SL coating. Also, the inner oxide band (layered) appear to be on average thicker in SL coating than in the NL coating. This suggests the outer oxide band characterized by larger crystallites that is found growing on the NL CrN–NbN coating is better at passivating the surface of the oxidizing cladding.

The STEM-EDS maps of the two oxide scales are very useful in understanding the nature of the oxide sub-bands. In both cases, the outer oxide layer seems to have lower concentrations of Cr than the inner oxide. Some Cr signal can be collected from this outer band, but Nb and Ni (impurity) seems to be the main component of the oxide crystallites. The inner band, instead, shows alternating regions of higher Cr concentration and lower Cr concentration. Where the Cr concentration is lower, the Nb map shows a higher signal suggesting the CrN–NbN layered structure is somehow reflected in the inner oxide chemistry. Ni seems to be coupled with the Nb in the inner oxide as well. O appears distributed uniformly across the oxide scale, and small regions of N enrichment can be found. A STEM-EDS line scan across the oxide scale of the SL CrN–NbN coating is presented in Fig. 7. From this analysis the O

concentration is measured ranging between 40 and 60 at.% depending on the region. Significant amounts of residual N are measured in the oxide, and up to 70 at.% N can be found in the portion of unoxidized CrN–NbN coating adjacent the oxidation front. This is possibly due to the accumulation of N freed during the oxidation which tends to migrate into the nitride. Ni, again, seems to concentrate together with Nb. The periodicity in the EDS signal might be identified as chemical changes across layers but it is impossible to distinguish the signal from noise.

EELS line scans performed on the exposed NL coating can be found in Fig. 8 for both the layered, inner band of the oxide, and for the coating immediately underneath the oxide scale. In the oxide, Cr and Nb EELS signal are in antiphase, where Cr has high signal Nb has low and vice versa. The O signal oscillates too, and it tends to be higher in correspondence to high Nb signal. The N signal is low and constant across the line scan but there are two bumps that suggest incomplete oxidation of some of the layers. In the case of the unoxidized NL coating (Fig. 8(c) and (d)), the Cr and Nb signals are in antiphase, and the N signal is higher in the Nb-rich layer. This suggests that N is not equally distributed between the Cr-rich and Nb-rich phases. The distance between peaks in Cr concentration in the oxide is almost twice the distance between peaks in the Cr signal from the coating. This suggests that a degree of volume expansion could be associated with the oxidation of the coating. The formation of pores could also be a co-cause of the increase in layer thickness.

X-ray diffractograms for as-deposited and autoclave exposed NL CrN–NbN coated cladding are displayed in Fig. 9. These show a strong signal from the Zr substrate, as well as broad peaks corresponding to the CrN and NbN phases. The contributions from CrN and NbN phases can be separated - as shown by the fitting of two contributions of the two most intense CrN and NbN peaks at $42°$ and $62°$ 2θ, respectively. In the
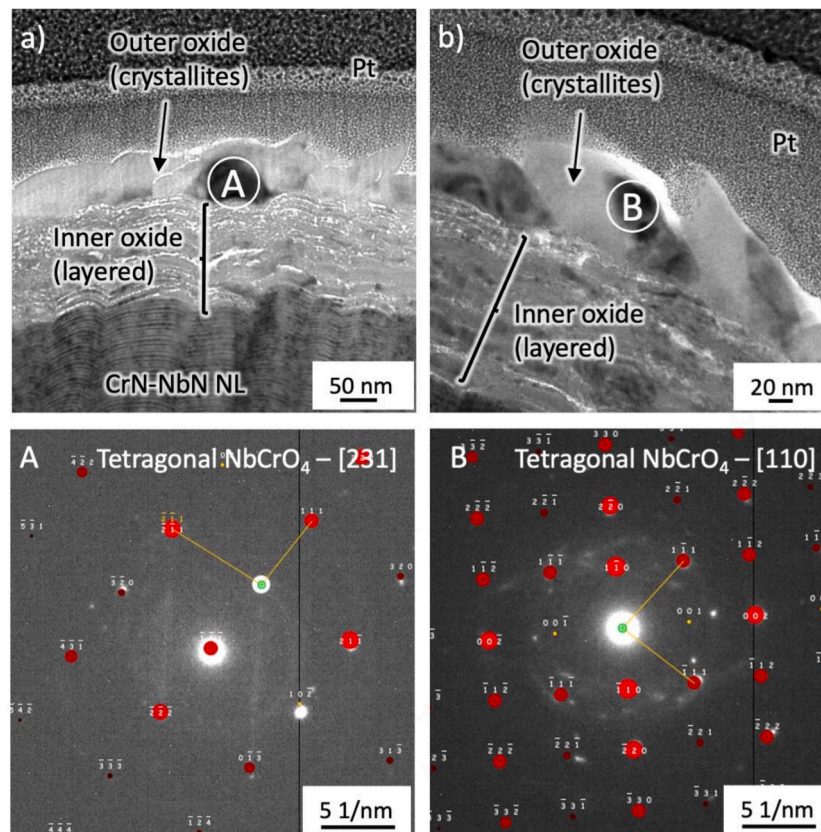
Fig. 4. BF-TEM of outer oxide scale grown on nanolayered CrN–NbN coatings ((a) and (b)). SADPs Pattern A and B were collected from crystallites in the outer surface are reported and were indexed as tetragonal $NbCrO_4$.
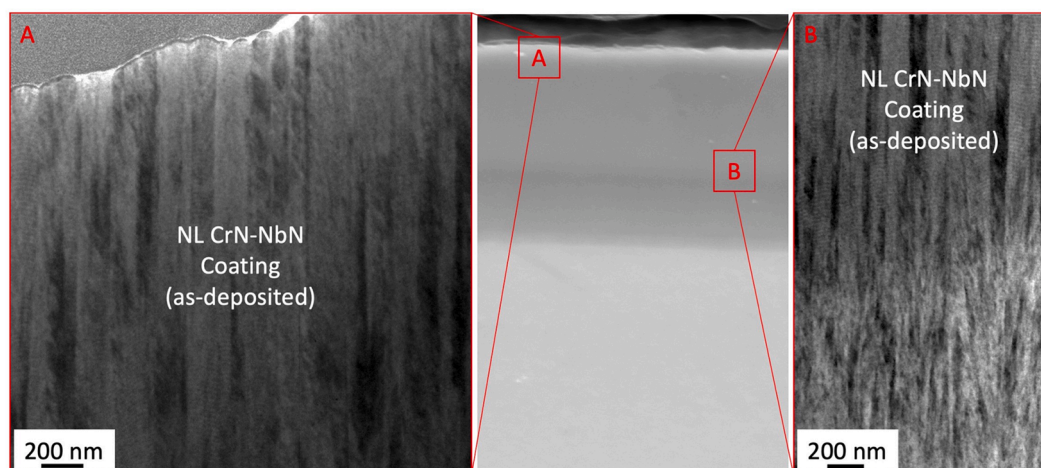

Fig. 5. SEM cross-section of as-deposited nanolayered CrN–NbN coating (Zr substrate is at the bottom of the image). Box A: BF-TEM image taken close to the outer surface of the coating. Box B: BF-TEM image taken where the coating changes in contrast.

case of the autoclave exposed NL CrN–NbN coated sample we also note the presence of additional peaks, the strongest one at $53.5°$, which can be associated with the tetragonal $CrNbO_4$ phase (confirmed by electron diffraction shown in Fig. 4). The presence of the $CrNbN_2$ ternary phase in the coating cannot be excluded due to a strong broadening of the peaks, while small secondary peaks possibly linked to Cr_3Nb_3N ternary phase are visible around the broad peak at $42°$

The x-ray diffractograms for as-deposited and autoclave exposed SL CrN–NbN coated claddings are reported in Fig. 10. As-deposited SL CrN–NbN shows mostly signal from the Zr phase, with minor contributions from the CrN–NbN coating (see zoomed-in Box A and Box B). It cannot be concluded whether the signal from the coating is from a homogeneous single phase, due to the low intensity of the signal. In the diffractogram from the autoclave exposed SL CrN–NbN a strong signal from the CrN–NbN coating is measured. This signal fits with a single set of peaks, indicating the presence of a homogenous $CrNbN_2$ ternary phase. Interestingly, in this sample the intensity of the peaks from the coating is much higher than that of the peaks from the Zr substrate - in contrast to the as-deposited sample. This might indicate that the crystallinity of the coating was improved by the autoclave exposure. After
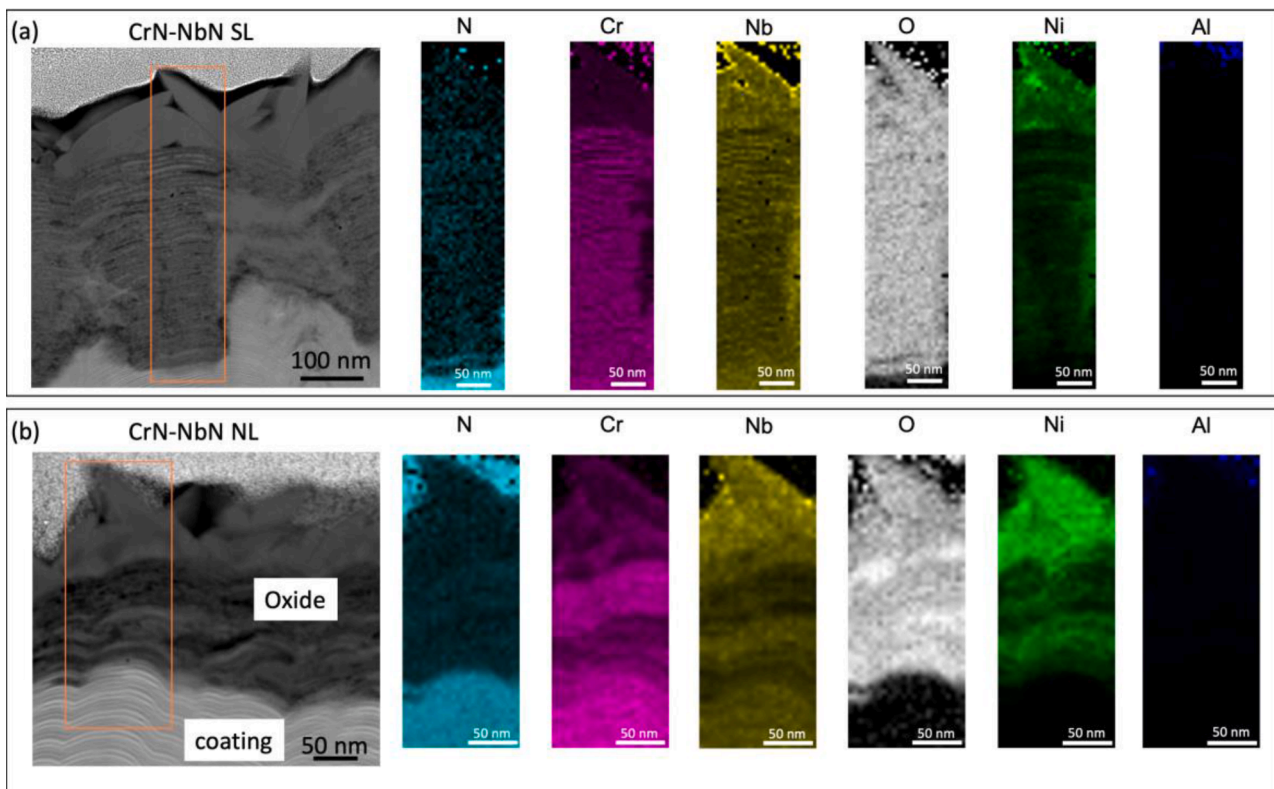
Fig. 6. STEM images and STEM EDS maps of the oxide scale found after autoclave exposure on the outer surface of superlattice CrN–NbN coating (a), and nano-layered CrN–NbN coating (b).
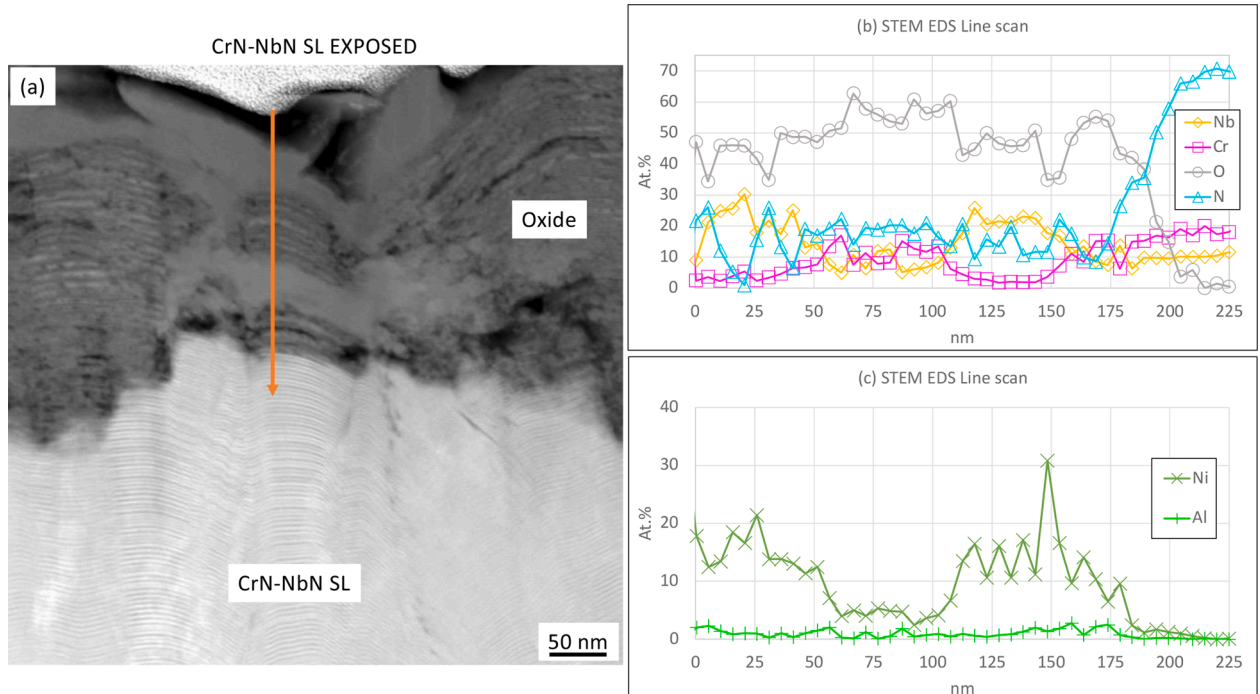

Fig. 7. STEM image of the superlattice CrN–NbN coating outer surface after autoclave (a) and STEM EDS line scan across the oxide scale (b). Ni and Al contamination originating from the autoclave are also observed (c).

exposure, a minor peak linked to the $NbCrO_4$ can be found, as displayed in Fig. 10 (Box C).

3D reconstructions of APT data collected from the bulk of SL and NL CrN–NbN coatings as-deposited and after autoclave exposure are presented in Fig. 11. Here the difference between the SL and NL layer thickness and uniformity becomes more visible. In the SL CrN–NbN coating the alternating layers have the same thickness and they appear almost flat at this scale. The layers in the NL coating are not only thicker
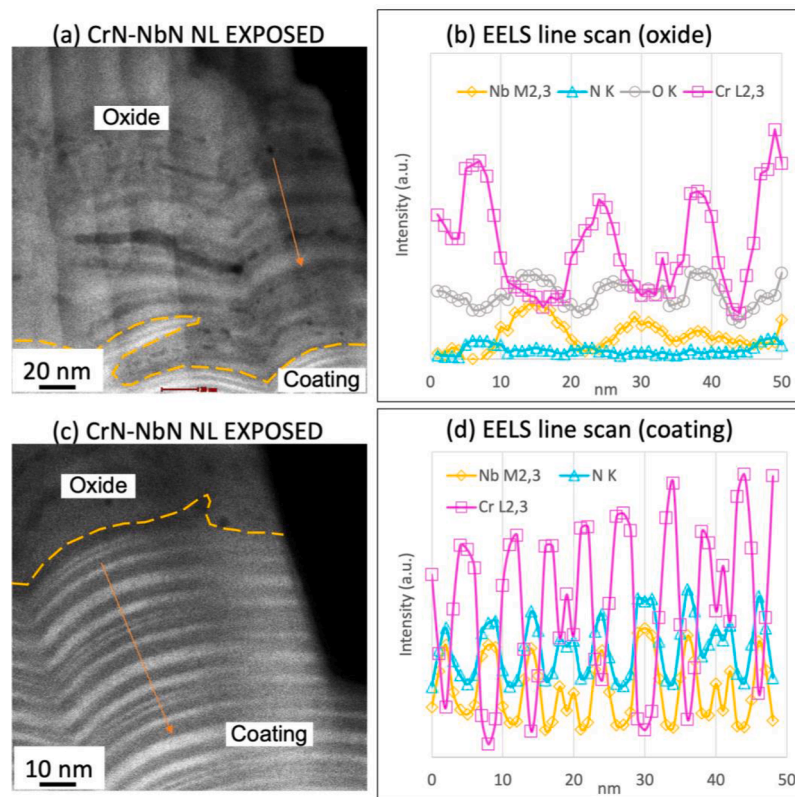
Fig. 8. STEM images of the outer surface of the nanolayered CrN–NbN coating after autoclave (oxide (a) and coating adjacent to the oxide (c)). EELS line scans perpendicular to the layers visible in the oxide (b) and in the coating (d).

on average but less homogeneous and more jagged. The columnar grains shown in the BF-TEM images of the NL coating were about 50 nm wide. Vertical structures with a similar size are also visible in the APT data (marked with a dashed line). In proximity of these grain boundaries the layers form kinks, resulting in an overall curvature of the layers. As a consequence, the layers in the NL coating appear as arches or as half domes, and this is visible in the boxes in Fig. 11(c) and (d), and in the previously presented BF-TEM and STEM images.

Some defects and inhomogeneities can also be found in the SL coating, but these imperfections are relatively minor and consist of small shifts in layer ordering (see Fig. 11(a) and (b)). These differences in morphology are also reflected in the chemical composition of the layers. In Fig. 12, 1D concentration profiles calculated in a direction perpendicular to the layers for the SL and NL CrN–NbN coatings as-deposited and exposed are plotted. For the SL coating, the periodicity is confirmed to be around 5 nm (each individual layer is about 2–3 nm thick). The composition of the Cr-rich and Nb-rich layers measured with APT is reported in Table 2. After exposure, the chemistry of the layers does not change greatly, but some homogenization of Cr and Nb across the layers might have occurred. In the case of the NL coating, there are more than two clear-cut compositions, and some areas with intermediate composition do exist. Nonetheless, a Cr-rich and a Nb-rich layer can be observed, and their composition is reported in Table 2. The Cr-rich layers are in general thinner (around 4–5 nm), while the Nb-rich layers appear thicker (around 6–8 nm). This is likely an artifact caused by the different evaporation fields of the two materials that can produce local magnification effects. A better idea of the layer thickness is obtained from the TEM and STEM data. No significant changes can be discerned after the autoclave exposure, and both coatings seem to be unaffected. Very small changes can be observed, and it is important to keep in mind that local variations in the coating chemistry might be behind these differences rather than actual changes due to the exposure.

APT reconstructions of the volume around the coating-substrate

interface of the SL CrN–NbN coated cladding before and after exposure are presented in Fig. 13. In the as-deposited SL coating-cladding interface it is possible to see the Cr bonding layer in the middle of the reconstruction with the nitride coating and Zr substrate at the two opposite sides of it. The Cr-nitride interface is sharp with some jagged steps that are probably due to some Cr grains sticking out. The change in composition at this interface is presented in Fig. 14(a). The chemical composition goes from 100 at.% Cr to 45 at.% N, 35 at.% Cr, and 20 at.% Nb in a few nanometers. The Cr-Zr phase interface is smooth and sharp, and some O and N can be found at it. As shown in Fig. 14(b), there is a 10 nm thick region where Cr, Nb, Zr, O and N are all found together at the interface. Cr and Zr composition profiles are flat in this 10 nm region and represent 45 at.% and 20 at.% of this layer, respectively. The Nb and N peak at 10 at.% and 20 at.% close to the Cr side, respectively. O is instead higher close to the Zr side where it reaches around 15 at.%. Another interesting feature that can be observed in Fig. 13(a) is the presence of O-enriched grain boundaries at the former surface of the Zr. These grain boundaries extend into the Zr-substrate for about 30–40 nm and are probably signs of the grinding and polishing performed on the Zr cladding surface before depositing the nitride coating. After exposure to autoclave, the Cr-nitride interface maintains a similar appearance but it is possible to see that some roughening of the Cr bonding layer is ongoing. The chemical composition of the interface, presented in Fig. 14 (c), does not change significantly but N depletion close to the Cr side seems to be occurring. Additionally, Cr seems to be diffusing out of the Cr bonding layer into the nitride coating, creating a faint enrichment of Cr in the area close to the interface with the Cr. More distinct evolution can be observed in the chemistry of the Cr-Zr interface shown in Fig. 14 (d).

The 10 nm region where Cr, Zr, N, O and Nb were all present before exposure has now grown to about 30–35 nm in thickness. The Cr content is 45 at.% adjacent to the Cr and decreases gradually down to 30 at.% before going sharply down to about 10 at.% once the Zr substrate is
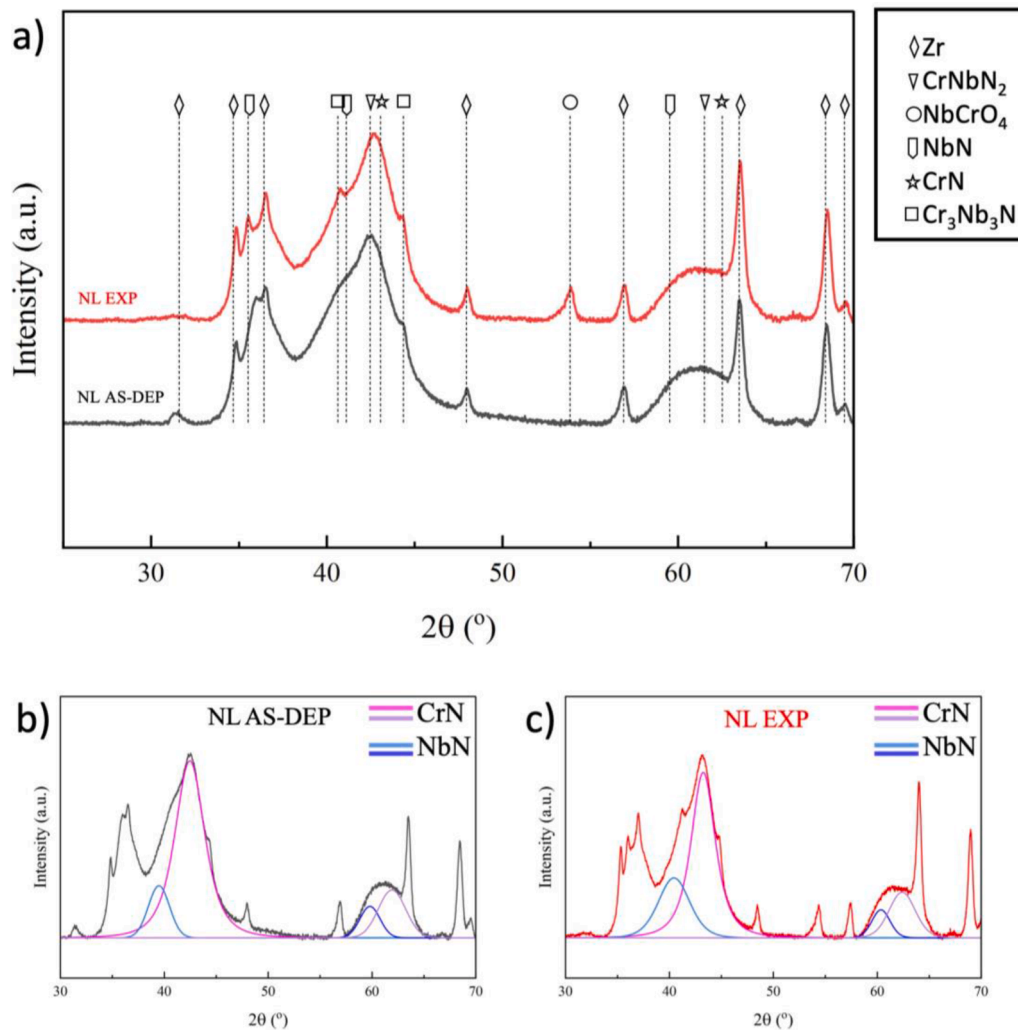
Fig. 9. (a) X-ray diffractograms for as-deposited nanolayered CrN–NbN coated Zr-cladding (black line), and autoclave exposed nanolayered CrN–NbN coated Zr-cladding (red line). (b) Deconvolution of main peaks from the as-deposited coating into CrN and NbN Gaussian peaks. (c) Deconvolution of main peaks from the autoclave exposed coating into CrN and NbN Gaussian peaks.

reached. Zr starts at about 20 at.% near the Cr side, and it increase up to 50 at.% before reaching the Zr substrate. N peaks at 20 at.% near the Cr (same as before exposure), but it now decreases more slowly down to 5–8 at.% before dropping to almost zero once the Zr substrate is reached. No new Nb seems to have reached the interface, but Nb is now distributed homogeneously throughout the mixed region. O appears to have been pushed out of this mixed region into the Zr substrate. Around 4–5 at.% of O can still be measured across the entire thickness of the mixed region. Less than 400 ppm Fe was measured at the Cr-Zr interface both before and after autoclave exposure.

4. Discussion

4.1. Corrosion resistance in BWR autoclave

The CrN–NbN coatings tested in this work were found to be able to survive the BWR water chemistry. Both versions of the coating developed an oxide scale of about 200–300 nm thickness that appears to be able to passivate the coating surface and prevent further oxidation. Both the SL and NL CrN–NbN coatings developed an oxide characterized by two main sub-bands: an outer oxide scale composed of crystallites 20–50 nm in size, and an inner layered band that conserved the layered morphology of the original coatings. This substructure was significantly better defined in the NL coating. In the SL coating it was sometimes

possible to find larger crystallites in the inner band. This oxide inner band was on average thicker in the SL than in the NL coating and its thickness was significantly less homogeneous in the oxidized SL coating. Cr and Nb were coexisting in both sub-bands, but the outer oxide was relatively richer in Nb, while Cr was dominant in the inner oxide. Ni could also be found predominantly in the outer oxide. Ni is an impurity originating from the autoclave environment and its presence in the outer scale suggests that this oxide has grown through a process of dissolution and precipitation rather than as direct oxidation of the substrate. The presence of this Ni impurity does not compromise the validity of this corrosion study: Ni and Fe impurities are in fact typical of all LWR environments, and can often be found forming crud on the surface of cladding tubes exposed to reactor environment [35,36]. The inner oxide, instead, preserved the layered structure of the coating and it has most likely formed through direct oxidation of the layered nitride coatings.

The outer oxide scale is mainly composed of 20–50 nm large crystallites that were indexed as tetragonal $NbCrO_4$. Signal from this phase could be measured with XRD in both exposed samples. The stoichiometric O content for this phase is 66.67 at.%, which is higher than the 50–65 at.% content measured by STEM-EDS on the SL oxide scale. This mismatch can be explained by the presence of residual N sitting in the anionic site of the $NbCrO_4$ crystal lattice [37–39]. The presence of Ni in the outer oxide scale is confirmed by STEM-EDS maps. This element must be dissolved in solid solution in the $NbCrO_4$ lattice eventually
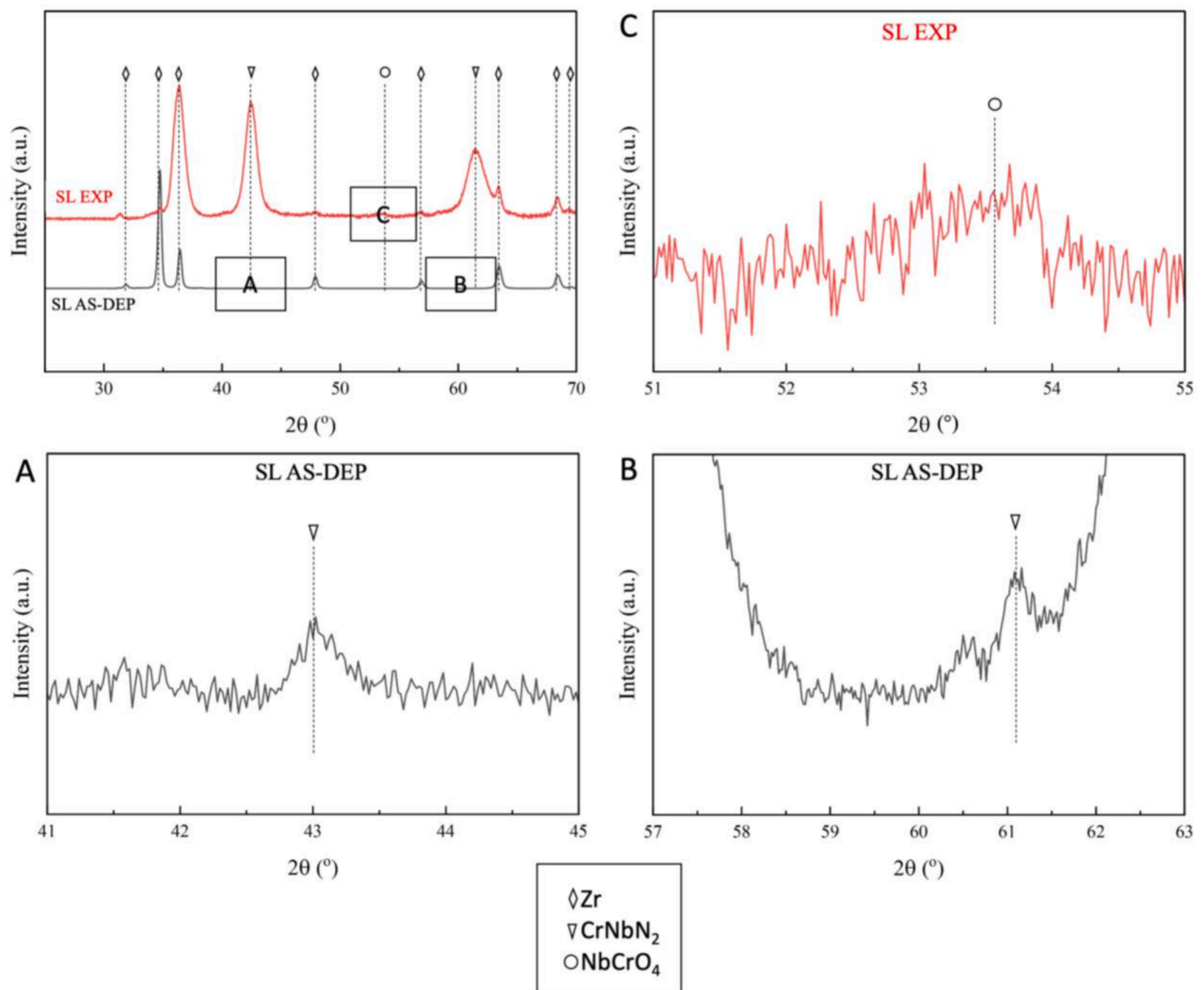
Fig. 10. X-ray diffractograms for as-deposited superlattice CrN–NbN coated Zr-cladding (black line), and autoclave exposed superlattice CrN–NbN coated Zr-cladding (red line). Zoomed-in boxes A and B display $CrNbN_2$ peaks in the diffractogram of as-deposited SL coating. Zoomed-in box C displays $NbCrO_4$ main peak in the diffractogram of the autoclave exposed SL coating.

substituting the Cr. Overall, EDS and STEM-EDS analysis reveal all three elements are present in the outer oxide, which suggest a complex oxide chemistry.

Understanding the chemistry of the inner oxide is more challenging. The EELS line scan through the inner oxide grown on the NL coating is presented in Fig. 8(b). The plot shows one family of layers where almost only Cr signal is present and another set of layers where both Nb and Cr are present. This subdivision is not universal and it is difficult to imagine what could be the situation for the SL coating which has much thinner layers and more chaotic subdivision in inner and outer oxide. In any case, the most likely phases forming the oxide layers on the NL coating are chromia for the Cr-rich layer and $CrNbO_4$ oxide for the Nb-rich layer. Other oxides could also be present, particularly in the regions where O and Nb signals are both seen increasing in comparison to the Cr-rich oxide, but the absence of clearly defined crystallites renders impossible the identification of these phases through electron diffraction or XRD. The oxidation of the coating layers seems to occur with significant volume expansion. As it is shown in the EELS line scans reported in Fig. 8, the distance between two Cr peaks in the oxide scale is around twice the distance between Cr peaks in the unoxidized coating.

Assuming the expansion is happening only along the oxide growth direction, this would imply a volume change by a factor of 2. The volume expansion for the Cr_2N to Cr_2O_3 phase transformation is by a factor 1.65. Considering that the formation of pores could exacerbate this expansion, a volume increase of about 2 times is somehow compatible. However, it is important to point out that the preferential dissolution and reprecipitation of one layer type over the other could have caused the redistribution of certain elements. This renders reconstructing the actual oxidation process very challenging.

One additional complication is the presence of N in the oxide. N is known to be able to substitute O anions in the lattice of mixed oxides (for example in spinel oxide) [37–39]. A few percent of N (5–7 at.% from bulk analysis) were measured in the oxide scale of both coatings, and the STEM-EDS line scan through the oxide scale developed on the SL coating shows up to 10–20 at.% of residual N after oxidation. Increased amounts of N are also measured in the portion of unoxidized coating adjacent to the oxide scale. All considered, it appears the oxidation of the coating transforms the CrN–NbN lattices into oxides with significant residual content of N. The N that cannot be hosted in the newly formed oxide lattice is instead pushed into the neighboring unoxidized coating
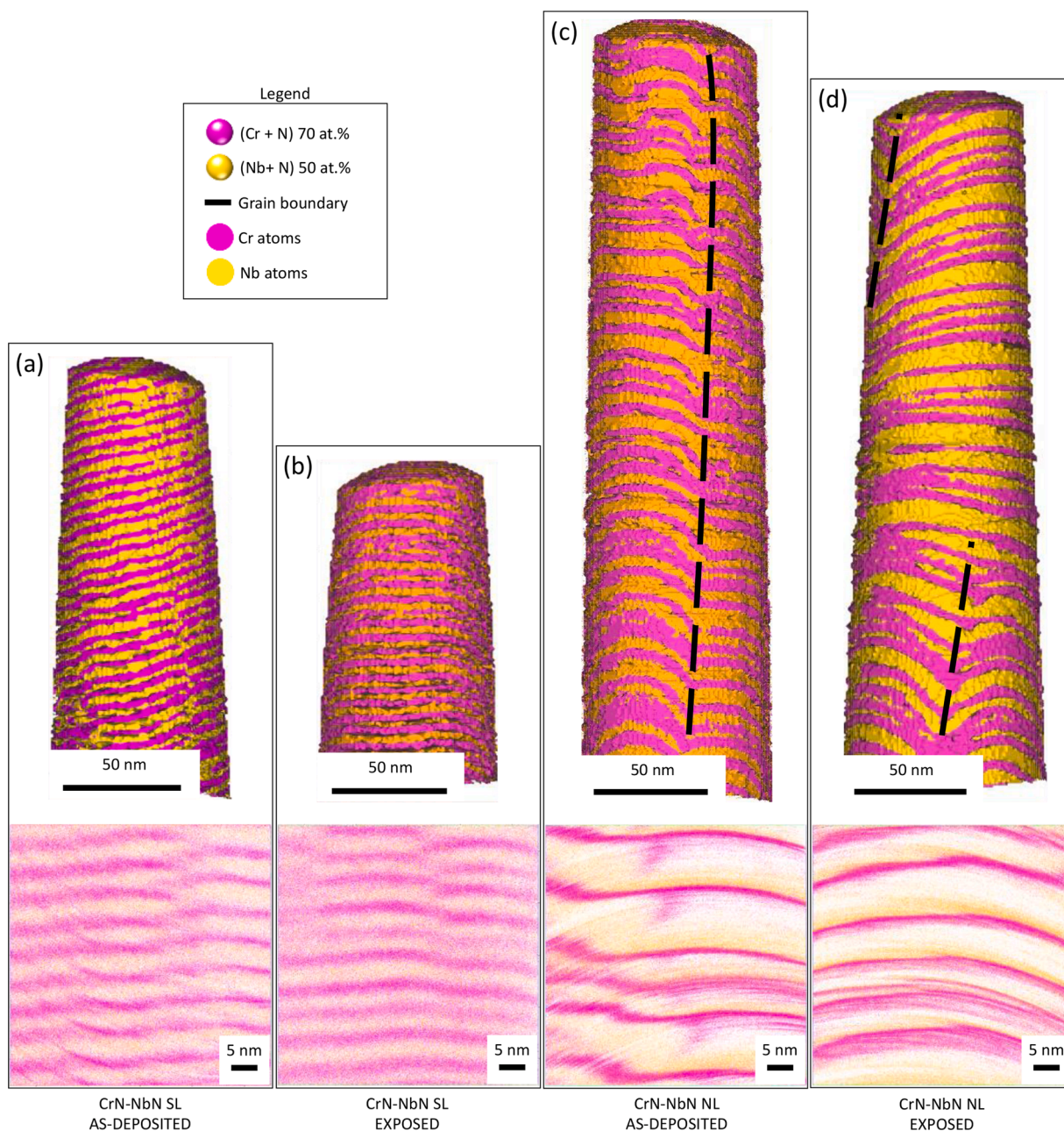
Fig. 11. 3D reconstructions of APT data collected from the bulk of the coatings. Superlattice CrN–NbN coating before (a) and after (b) autoclave exposure, and nanolayered CrN–NbN coating before (c) and after (d) autoclave exposure. Top figures present isosurfaces calculated at Cr plus N at 70 at.% (magenta) and Nb plus N at 50 at.% (orange). Bottom figures: $50 \times 50 \times 20$ nm^3 boxes perpendicular to the layers.

causing an increase in the N content in the CrN–NbN phases. The residual N in the oxide scale can also be used to explain the relatively low O concentration measured with STEM-EDS as mentioned above.

Overall, the formed oxide scale seems to be excellent at protecting the substrate from further oxidation and it is able to passivate the surface of the coating. The division into two sub-bands of oxide could be playing an important role in the effectiveness of this oxide scale. The outer oxide appears to protect the inner oxide by decreasing the activity of oxygen that manages to penetrate to the inner oxide, and by circumventing the dissolution of any chromia formed underneath. This protection mechanism and oxide scale morphology are very common in stainless steels and Ni-alloys [11,40,41]. Additionally, the layered morphology of the coatings could be forcing the oxidation front to proceed layer by layer requiring the nucleation of different oxides for each new layer oxidized, thus slowing down significantly the oxidation rate.

In terms of performance, the SL and NL coatings were almost the same: both formed a stable oxide about 200–300 nm thick and no further transformation of the underlying coating could be observed. Nonetheless, the NL CrN–NbN has displayed a few features that might bring some potential benefits for longer exposure times. The outer oxide scale of the NL CrN–NbN coating appears to be more developed and presents larger crystallites on average. Other characteristics that point in the same direction are the smooth oxide-coating interface and the uniformity in thickness. The oxide-coating interface of the NL CrN–NbN coating is significantly flatter and more regular than the oxide-coating interface of the SL CrN–NbN coating. The oxidation front appears to progress in a slow and controlled way. As a result, the oxide thickness is almost the same everywhere it is measured. In the case of the SL coating, the oxide-coating interface presents significant steps and kinks. This would suggest that the oxidation front is progressing faster in certain areas than in
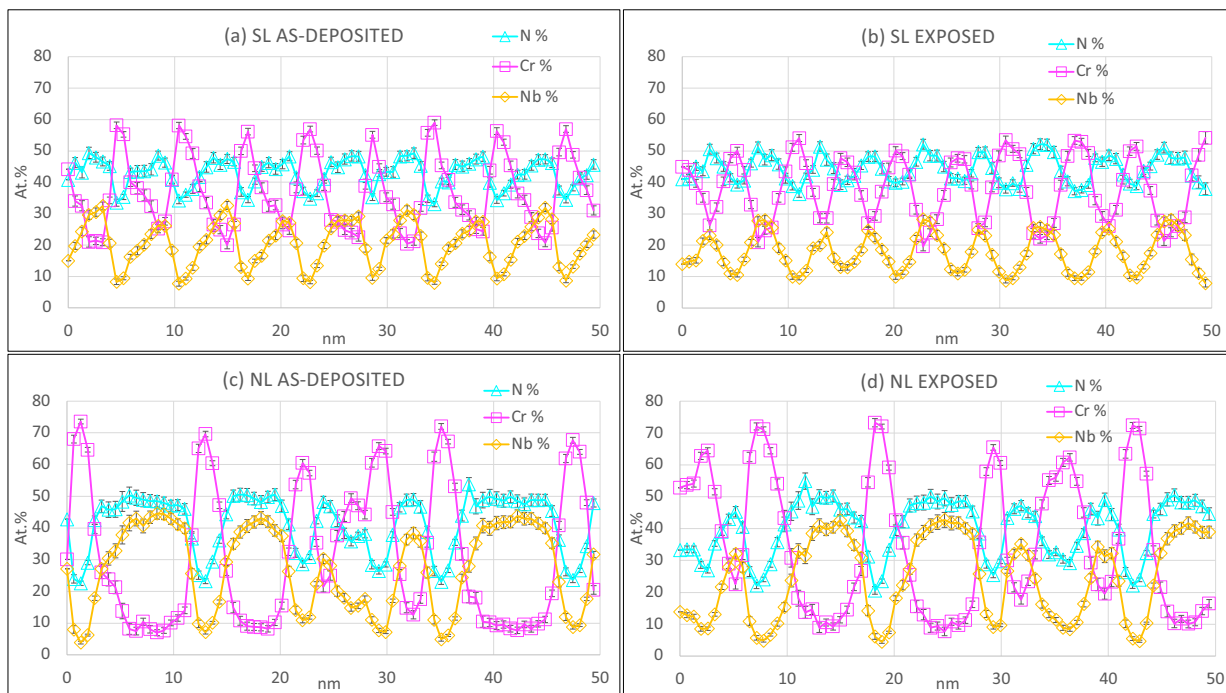
Fig. 12. 1D concentration profiles across coating layers. Layer composition in superlattice CrN–NbN coating before (a) and after (b) autoclave exposure. Layer composition in nanolayered CrN–NbN coating before (c) and after (d) autoclave exposure.

Table 2
Approximate composition of the layers constituting the SL and NL CrN–NbN coatings, from APT.

Coating	Layer type	Cr (at.%)	Nb (at.%)	N (at.%)
SL CrN–NbN (as-deposited)	Cr-rich	55–60	8–9	33–35
	Nb-rich	20–25	28–33	47–50
NL CrN–NbN (as-deposited)	Cr-rich	68–72	5–10	22–28
	Nb-rich	9–10	40–45	48–50

other, contributing to the uneven thickness of the oxide. The main difference between the SL and NL CrN–NbN is the thickness of the layers they are made of. Thicker layers might promote the formation of larger crystallites and result in a more well-defined subdivision of the oxide

scale. It is also true that the layers of the SL and NL do not have the exact same composition, and this could be also playing a role. Overall, the application of the tested nitride coatings provided a significant improvement in oxidation resistance compared to uncoated claddings tested under similar circumstances [42].

4.2. Composition and phases forming the SL and NL CrN–NbN layers

Using APT data it was possible to determine with relatively high accuracy the composition of the different layers deposited to form the coatings. In the SL CrN–NbN coating, the Cr-rich layer has a metal-nitrogen ratio that resembles a $(Cr,Nb)_2N$ phase with 33 at.% N, 58–60 at.% Cr, and 7–9 at.% Nb. The Nb-rich layer is instead closer to a $(Nb,Cr)N$ structure with 50 at.% N, 25–30 at.% Nb, and 20–25 at.% Cr.
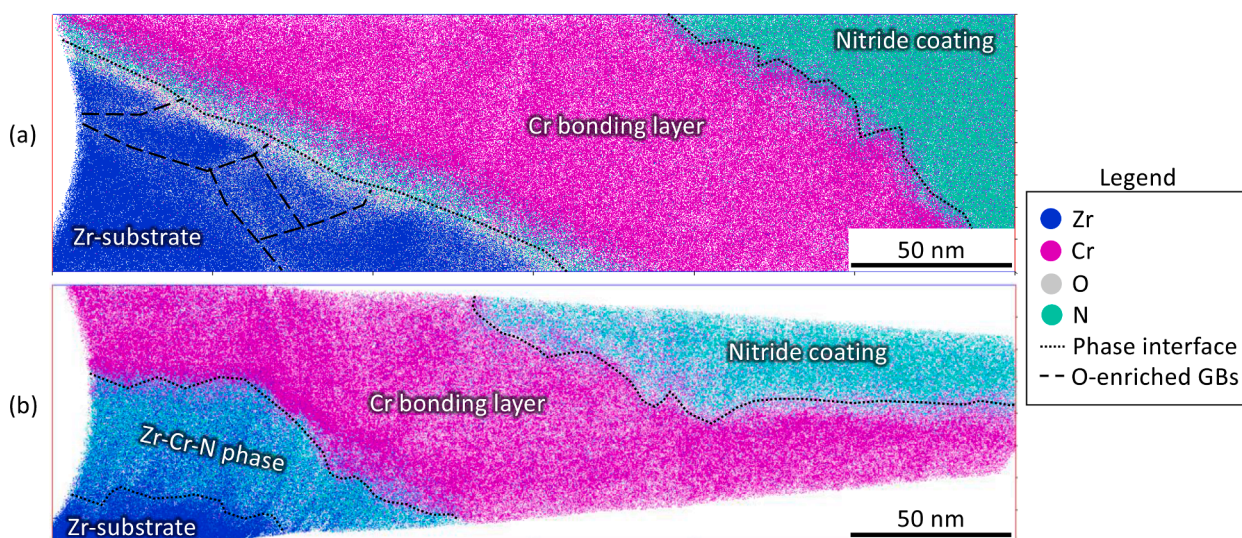

Fig. 13. 3D reconstructions of APT data collected at the coating-substrate interface of the cladding coated with superlattice CrN–NbN coating: as-deposited (a) and after autoclave exposure (b). Size of the boxes $300 \times 80 \times 50$ nm^3.
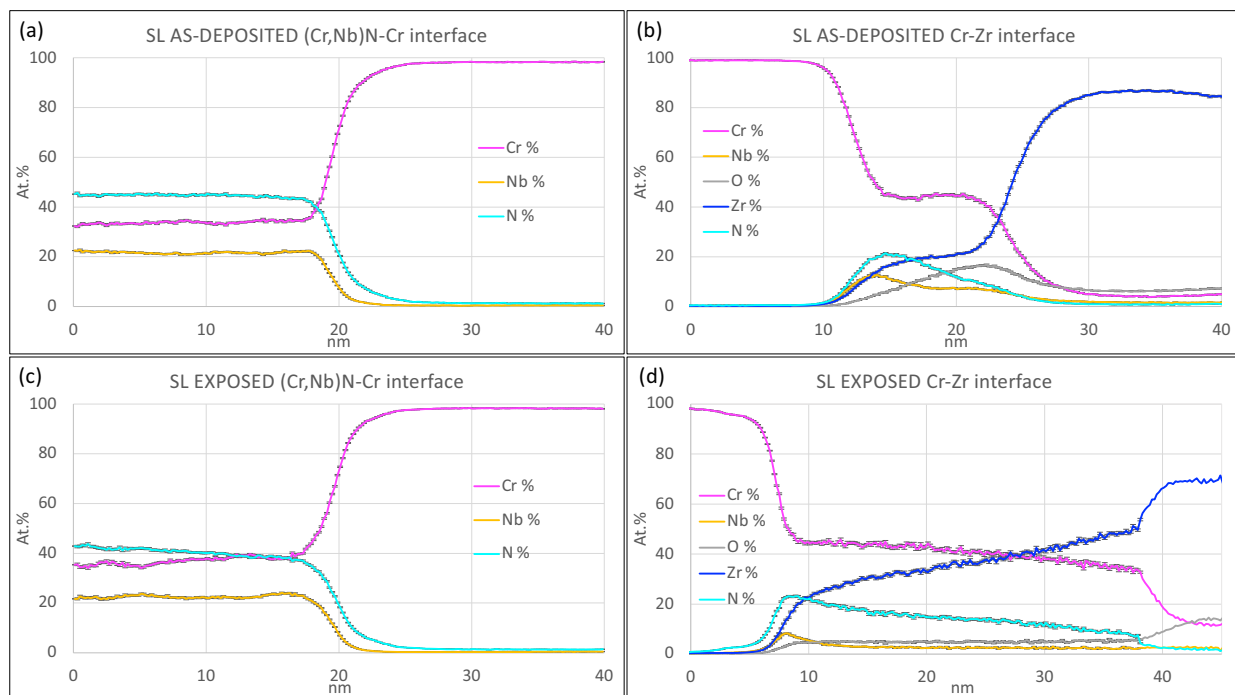
Fig. 14. Composition profiles (proxigrams) calculated across the coating-substrate interface of a cladding coated with superlattice CrN–NbN coating: as-deposited ((a) and (b)), and after autoclave exposure ((c) and (d)). The interface between the nitride coating and the Cr bonding layer is presented to the left, while the interface between the bonding layer and the Zr-substrate is presented to the right.

This would suggest the coating is composed by two alternating phases. After the exposure to autoclave, the Cr content in the Cr-rich layers seems to be slightly lower, while the Nb content in the same layer increases slightly, as if the two different layers were starting to mix. The change is very small though, and it might be attributed to local variations. The XRD data for the as-deposited SL shows very weak peaks that could match a combination of CrN, NbN, and $CrNbN_2$ ternary phase. The low intensity of these peaks indicates that the crystallinity of the as-deposited SL coating is extremely low. The low deposition temperature typical of MS-PVD in combination with the ionic bombardment utilized to guarantee elevated coating densities when depositing nitride coatings [43,44] could be the main explanation for this low crystallinity. The XRD results for the exposed SL coating show clear, gaussian peaks corresponding to the $CrNbN_2$ ternary phase. This implies that the 60 days at 300 °C allowed the coating to increase significantly its crystallinity, either by annihilation of 1D defects induced during deposition or by allowing short-range diffusion and rearrangement of atoms. According to the XRD diffractometry, the chemical variation of the layers measured with APT does not reflect two different alternating crystal lattices, but rather a single $CrNbN_2$ crystal lattice with significant periodic variations in composition that result in the emergence of the superlattice layered structure. This would be particularly true for the SL coating after the autoclave exposure. On this note, the small chemical changes measured with APT in the layer composition after exposure could be linked to the increased crystallinity measured with the XRD.

Less clear is the nature of the phases present in the NL CrN–NbN coating. The APT data showed Cr-rich layers composed of 70 at.% Cr, 5 at.% Nb, and 25 at.% N; and Nb-rich layers composed of 40 at.% Nb, 10 at.% Cr, and 50 at.% N. The Cr-rich layers could fit reasonably well with the $(Cr,Nb)_2N$ stoichiometry. Even if the metallic content of these layers is higher than the precise stoichiometry, Cr_2N is known to have a wide range of stable compositions, particularly at elevated temperatures, and it is possible that the Cr-rich layer is metastable at room temperature but was still able to form during deposition. The composition of the Nb-rich layers fits well with a $(Nb,Cr)N$ stoichiometry. From the XRD analysis emerges that the main crystalline phases present in the NL coatings are

CrN and NbN. Hence, the Nb-rich layers must be arranging into a NbN lattice, which fits quite well their chemical composition, while the Cr-rich layers must form a CrN crystal lattice despite the significant deviation from the CrN stoichiometry. Secondary peaks relative to Cr_3Nb_3N and possibly $CrNbN_2$ were also measured and could partially explain this inconsistency. No real difference is found in the NL layers composition before and after autoclave both in APT and XRD data, which means that 300 °C is not sufficient to allow significant diffusion of Cr out of the supersaturated CrN lattice. An alternative explanation could be that adding Cr atoms to the Nb-rich layer would come at an energy cost, leaving the Cr trapped inside the Cr-rich layer.

Overall, both coatings have demonstrated to be stable at this temperature. It is safe to assume that the diffusion rates of Cr and Nb in the nitride lattice are too low to produce any significant change in the chemistry of such coatings at operating temperature. However, irradiation could promote mixing of the layers, particularly in the thinner layers of the SL coating.

4.3. Evolution of the coating-substrate interface during autoclave exposure

The coatings are very stable in autoclave at 300 °C, but some interaction does occur between the substrate and the coating during exposure, as is shown by the APT data displayed in Figs. 13 and 14. At the coating-substrate interface of the SL CrN–NbN as-deposited coated cladding two main features are evident: the presence of a Cr bonding layer (deposited intentionally during deposition), and the presence of what is left of the Zr-cladding native oxide. The native oxide was present on the outer surface of the cladding before the deposition of the nitride coating. Plasma cleaning was performed before deposition to prepare the substrate surface, but a small amount of residual oxidized Zr can still be found buried at the interface with the coating. At the initial stages of deposition, some Cr, Nb, and N end up mixing with this native oxide forming a 10 nm thick mixed region. This region evolved significantly during the time in autoclave, and it is found growing to about 30–35 nm in thickness. The main elements promoting the formation and growth of

this phase are N and Cr. N has to come from the nitride coating, and it must have diffused through the Cr bonding layer in order to get to the Zr substrate. This would explain the N depletion zone seen after exposure in the proxigram across the Cr-nitride interface plotted in Fig. 14c. The reaction between Zr and N has been documented for nitride coated claddings tested at elevated temperatures [45,46], and it is reasonable to imagine that the mixed region reported in this work could easily evolve into ZrN at higher temperatures. The diffusion of Cr into Zr is very well documented in the case of Cr coated claddings and it has been reported even at operating temperatures [47]. Coupled with the intermixing between Cr and Zr, Fe is often found enriching in the mixed region. In this material, though, almost no Fe could be detected at the Cr-Zr interface. This could be linked to the abundance of N diffusing from the coating to the substrate which reacts with the Zr leading to the formation of ZrN. The presence of this ZrN phase was found hindering the Cr-Zr reaction [46] which could explain the absence of Cr_2Zr laves phase or Fe-enrichment at the interface. The formation of this Zr-Cr-N phase was visible in BF-TEM images of the SL CrN–NbN coating-substrate interface (see Fig. 2), but no nucleation of this phase was seen occurring for the NL CrN–NbN coating. This is probably due to the thickness of the Cr bonding layer used in the NL coating (250 nm in the NL coating vs 50 nm in the SL case), which, being five times thicker, must have delayed the diffusion of N from the nitride to the Zr substrate.

5. Conclusions

In this work, a superlattice (SL) CrN–NbN coating and a nanolayered (NL) CrN–NbN coating were deposited onto Zr claddings made of HiFi™ alloy. These coated claddings were then exposed to autoclave corrosion testing. The as-deposited materials and the samples exposed to autoclave were analyzed with a wide range of advanced characterization techniques and the main results and conclusions are reported below:

(1) Both the SL and NL CrN–NbN coating survived the exposure to BWR water chemistry in autoclave. Both coatings formed a 200–300 nm thick passivating oxide which represents a significant improvement when compared with uncoated claddings [42]. The oxide scale was subdivided into an outer scale characterized by 20–50 nm large crystallites of $NbCrO_4$ (with Ni impurities), and an inner oxide scale formed by alternating layers of Cr-rich and Nb-rich oxides. Traces of N could still be measured with EDS in the formed oxide.

(2) Despite the nanoscale of the layering in the coatings, the morphology and chemistry of the two coatings were not modified by the exposure, and no significant mixing was observed. The coatings have demonstrated to be stable at BWR operating temperature.

(3) In the case of the SL CrN–NbN coated HiFi™ cladding, some Cr and N were found to diffuse from the coatings into the substrate. The diffusion of these two elements caused the nucleation and growth of a 30–35 nm thick Zr-Cr-N phase arranged into a discontinuous band along the coating-substrate interface, and growing into the Zr substrate. This phase is expected to evolve into a ZrN for exposures at higher temperature.

(4) The thicker layers of the NL CrN–NbN coating appear to have promoted the formation of an oxide scale characterized by more defined oxide bands: outer protective oxide and inner layered oxide. This subdivision was visible on the SL CrN–NbN coating as well but it was less clearly developed. Additionally, the oxide-coating interface was flat in the NL coating and while it was quite rough and uneven for the SL coating. The morphology of the oxide found on the NL coating appears generally more desirable. The difference in thickness of the layers that characterize the two coatings seems to be responsible for the differences reported in the oxidation mechanism.

(5) The thicker Cr bonding layer employed at the coating-substrate interface in the case of the NL CrN–NbN coating was able to delay the formation of the Zr-Cr-N phase described in point (3). This suggests that the thickness of such bonding layers can affect the diffusion of N from the coating into the substrate and hinder the interaction of N with Zr.

CrN–NbN nanolayered coatings performed well in simulated BWR environment and are very promising candidates as ATF material for BWRs. Further optimization of the coatings can be performed and a deeper understanding of the effect of the layered structure could be obtained. The study of a monolithic nitride coating with the same average composition could help shed further light onto the effects of the layered morphology on the oxidation mechanism. Other nitride coatings have performed well under simulated accident conditions. However, high temperature corrosion studies in steam need to be performed on both SL and NL CrN–NbN in order to confirm the potential of these materials as ATF designs.

CRediT authorship contribution statement

Andrea Fazi: Investigation, Writing – original draft, Visualization, Conceptualization. **Mohammad Sattari:** Investigation, Methodology. **Michal Strach:** Investigation, Methodology. **Torben Boll:** Methodology. **Krystyna Stiller:** Writing – review & editing, Conceptualization. **Hans-Olof Andrén:** Writing – review & editing, Conceptualization. **Denise Adorno Lopes:** Conceptualization, Resources. **Mattias Thuvander:** Supervision, Project administration, Funding acquisition, Writing – review & editing, Conceptualization.

Declaration of Competing Interest

The authors declare that they have no known competing financial interests or personal relationships that could have appeared to influence the work reported in this paper.

Data availability

The atom probe datasets utilized in this work have been made available at figshare.com [48].

References

[1] R.B. Rebak, Accident-tolerant fuels cladding concept: coatings for zirconium alloys. Accident Tolerant Materials For Light Water Reactor Fuels, Elsevier, 2020, pp. 63–81, https://doi.org/10.1016/b978-0-12-817503-3.00004-3.

[2] R.B. Rebak, Worldwide development of accident tolerant fuels, areas of study, claddings, and fuels. Accident Tolerant Materials For Light Water Reactor Fuels, Elsevier, 2020, pp. 43–62, https://doi.org/10.1016/b978-0-12-817503-3.00003-1.

[3] S.J. Zinkle, K.A. Terrani, J.C. Gehin, L.J. Ott, L.L. Snead, Accident tolerant fuels for LWRs: a perspective, J. Nucl. Mater. (2014), https://doi.org/10.1016/j.jnucmat.2013.12.005.

[4] K.A. Terrani, Accident tolerant fuel cladding development: promise, status, and challenges, J. Nucl. Mater. 501 (2018) 13–30, https://doi.org/10.1016/J.JNUCMAT.2017.12.043.

[5] C. Tang, M. Stueber, H.J. Seifert, M. Steinbrueck, Protective coatings on zirconium-based alloys as accident-tolerant fuel (ATF) claddings, Corros. Rev. 35 (2017) 141–165, https://doi.org/10.1515/corrrev-2017-0010.

[6] J. Yang, M. Steinbrück, C. Tang, M. Große, J. Liu, J. Zhang, D. Yun, S. Wang, Review on chromium coated zirconium alloy accident tolerant fuel cladding, J. Alloys Compd. 895 (2022), 162450, https://doi.org/10.1016/j.jallcom.2021.162450.

[7] Y. Deng, W. Chen, B. Li, C. Wang, T. Kuang, Y. Li, Physical vapor deposition technology for coated cutting tools: a review, Ceram. Int. 46 (2020) 18373–18390, https://doi.org/10.1016/j.ceramint.2020.04.168.

[8] P.H. Mayrhofer, C. Mitterer, L. Hultman, H. Clemens, Microstructural design of hard coatings, Prog. Mater. Sci. 51 (2006) 1032–1114, https://doi.org/10.1016/J.PMATSCI.2006.02.002.

[9] J.W. Du, L. Chen, J. Chen, Y. Du, Mechanical properties, thermal stability and oxidation resistance of TiN/CrN multilayer coatings, Vacuum 179 (2020), 109468, https://doi.org/10.1016/J.VACUUM.2020.109468.

[10] A. Fazi, P. Lokhande, D.A. Lopes, K. Stiller, H.-O. Andrén, M. Thuvander, Comparing CrN and TiN coatings for accident-tolerant fuels in PWR and BWR autoclaves, J. Nucl. Eng. 3 (2022) 321–332, https://doi.org/10.3390/jne3040019.

[11] S. Tuzi, H. Lai, K. Göransson, M. Thuvander, K. Stiller, Corrosion of pre-oxidized nickel alloy X-750 in simulated BWR environment, J. Nucl. Mater. 486 (2017) 350–360, https://doi.org/10.1016/j.jnucmat.2017.01.051.

[12] J. Chen, B. Forssgren, J. Lejon, K. Fritioff, On the stability of oxides formed under BWR conditions: some observations on a stainless steel and nickel-base alloys, in: NPC 2012: Nuclear Plant Chemistry Conference, International Conference on Water Chemistry of Nuclear Reactor Systems, France, 2012, 46071832. http://inis.iaea.org/search/search.aspx?orig_q=RN.

[13] S. Mahboubi, H.S. Zurob, G.A. Botton, J.R. Kish, Effect of water vapour partial pressure on the chromia (Cr2O3)-based scale stability, Can. Metal. Q. 57 (2018) 89–98, https://doi.org/10.1080/00084433.2017.1373968.

[14] S. Mahboubi, Y. Jiao, W. Cook, W. Zheng, D.A. Guzonas, G.A. Botton, J.R. Kish, Stability of chromia (Cr2O3)-based scales formed during corrosion of austenitic Fe-Cr-Ni alloys in flowing oxygenated supercritical water, Corrosion 72 (2016) 1170–1180, https://doi.org/10.5006/1982.

[15] E. Bemporad, C. Pecchio, S. de Rossi, F. Carassiti, Characterisation and wear properties of industrially produced nanoscaled CrN/NbN multilayer coating, Surf. Coat. Technol. 188–189 (2004) 319–330, https://doi.org/10.1016/j.surfcoat.2004.08.069.

[16] Y.P. Purandare, A.P. Ehiasarian, P.E. Hovsepian, Deposition of nanoscale multilayer CrN/NbN physical vapor deposition coatings by high power impulse magnetron sputtering, J. Vac. Sci. Technol. A. 26 (2008) 288, https://doi.org/10.1116/1.2839855.

[17] J.A. Araujo, R.M. Souza, N.B. de Lima, A.P. Tschiptschin, Thick CrN/NbN multilayer coating deposited by cathodic arc technique, Mater. Res. 20 (2016) 200–209, https://doi.org/10.1590/1980-5373-MR-2016-0293.

[18] A. Garzon-Fontecha, H. Castillo, D. Escobar-Rincón, E. Restrepo-Parra, W. de La Cruz, Compositional and electrical properties of Cr, Nb, Cr/Nb, CrNbN, and CrN/NbN multilayers grown using the d.c. magnetron sputtering technique, Surf. Interface Anal. 51 (2019) 906–913, https://doi.org/10.1002/SIA.6664.

[19] D. Wang, Y. Fu, M. Hu, D. Jiang, X. Gao, Q. Wang, J. Yang, J. Sun, L. Weng, Effect of Nb content on the microstructure and corrosion resistance of the sputtered Cr-Nb-N coatings, J. Alloys Compd. 740 (2018) 510–518, https://doi.org/10.1016/J.JALLCOM.2018.01.034.

[20] K. Yamamoto, S. Kujime, K. Takahara, Properties of nano-multilayered hard coatings deposited by a new hybrid coating process: combined cathodic arc and unbalanced magnetron sputtering, Surf. Coat. Technol. 200 (2005) 435–439, https://doi.org/10.1016/J.SURFCOAT.2005.02.175.

[21] A. Illana, E. Almandoz, G.G. Fuentes, F.J. Pérez, S. Mato, Comparative study of CrAlSiN monolayer and CrN/AlSiN superlattice multilayer coatings: behavior at high temperature in steam atmosphere, J. Alloys Compd. 778 (2019) 652–661, https://doi.org/10.1016/j.jallcom.2018.11.199.

[22] J. Liu, Z. Hao, Z. Cui, D. Ma, J. Lu, Y. Cui, C. Li, W. Liu, S. Xie, P. Huang, G. Bai, D. Yun, Investigation of the oxidation mechanisms of superlattice Cr-CrN/TiSiN-Cr multilayer coatings on Zircaloy substrates under high-temperature steam atmospheres, Corros. Sci. 192 (2021) 109782, https://doi.org/10.1016/j.corsci.2021.109782.

[23] E. Alat, A.T. Motta, R.J. Comstock, J.M. Partezana, D.E. Wolfe, Multilayer (TiN, TiAlN) ceramic coatings for nuclear fuel cladding, J. Nucl. Mater. 478 (2016) 236–244, https://doi.org/10.1016/j.jnucmat.2016.05.021.

[24] Z. Li, C. Liu, Q. Chen, J. Yang, J. Liu, H. Yang, W. Zhang, R. Zhang, L. He, J. Long, H. Chang, Microstructure, high-temperature corrosion and steam oxidation properties of Cr/CrN multilayer coatings prepared by magnetron sputtering, Corros. Sci. 191 (2021) 109755, https://doi.org/10.1016/j.corsci.2021.109755.

[25] J. Liu, Z. Hao, Z. Cui, D. Ma, J. Lu, Y. Cui, C. Li, W. Liu, S. Xie, P. Hu, P. Huang, G. Bai, D. Yun, Oxidation behavior, thermal stability, and the coating/substrate interface evolution of CrN–coated Zircaloy under high-temperature steam, Corros. Sci. 185 (2021), 109416, https://doi.org/10.1016/j.corsci.2021.109416.

[26] H. Su, X. Wu, L. Wu, S. Zhao, Y. Zhong, Z. Ning, N. Liu, J. Yang, Effect of Nb content on microstructure, mechanical property, high-temperature corrosion and oxidation resistance of CrNb coatings for accident tolerant fuel cladding, Int. J. Refract. Metals Hard Mater. 110 (2023), 106010, https://doi.org/10.1016/j.ijrmhm.2022.106010.

[27] IAEA, TECDOC-709: fuel failure in normal operation of water reactors: experience, mechanisms and management, 1993.

[28] M. Kopeč, O. Pašta, M. Malá, P. Halodová, L. Cvrček, J. Krejčí, On debris-fretting impact—the study of oxide and chromium layer application, J. Nucl. Eng. Radiat. Sci. 7 (2021), https://doi.org/10.1115/1.4048239.

[29] R.B. Rebak, Current materials in light water reactors. Why do we need a materials renewal?. Accident Tolerant Materials For Light Water Reactor Fuels Elsevier, 2020, pp. 15–41, https://doi.org/10.1016/B978-0-12-817503-3.00002-X.

[30] Z. Karoutas, J. Brown, A. Atwood, L. Hallstadius, E. Lahoda, S. Ray, J. Bradfute, The maturing of nuclear fuel: past to accident tolerant fuel, Progr. Nucl. Energy 102 (2018) 68–78, https://doi.org/10.1016/j.pnucene.2017.07.016.

[31] D. Tomus, H.P. Ng, In situ lift-out dedicated techniques using FIB-SEM system for TEM specimen preparation, Micron 44 (2013) 115–119, https://doi.org/10.1016/j.micron.2012.05.006.

[32] R.M. Langford, M. Rogers, In situ lift-out: steps to improve yield and a comparison with other FIB TEM sample preparation techniques, Micron 39 (2008) 1325–1330, https://doi.org/10.1016/j.micron.2008.02.006.

[33] K. Thompson, D. Lawrence, D.J. Larson, J.D. Olson, T.F. Kelly, B. Gorman, In situ site-specific specimen preparation for atom probe tomography, Ultramicroscopy 107 (2007) 131–139, https://doi.org/10.1016/j.ultramic.2006.06.008.

[34] D. Mayweg, J. Eriksson, O. Bäcke, A.J. Breen, M. Thuvander, Focused Ion Beam induced hydride formation does not affect Fe, Ni, Cr-clusters in irradiated Zircaloy-2, J. Nucl. Mater. 581 (2023), 154444, https://doi.org/10.1016/J.JNUCMAT.2023.154444.

[35] J. Deshon, D. Hussey, B. Kendrick, J. McGurk, J. Secker, M. Short, Pressurized water reactor fuel crud and corrosion modeling, JOM 63 (2011) 64–72, https://doi.org/10.1007/s11837-011-0141-z.

[36] J. Henshaw, J.C. McGurk, H.E. Sims, A. Tuson, S. Dickinson, J. Deshon, A model of chemistry and thermal hydraulics in PWR fuel crud deposits, J. Nucl. Mater. 353 (2006) 1–11, https://doi.org/10.1016/j.jnucmat.2005.01.028.

[37] K.E. Sickafus, J.M. Wills, N.W. Grimes, Structure of spinel, J. Am. Ceram. Soc. 82 (2004) 3279–3292, https://doi.org/10.1111/j.1151-2916.1999.tb02241.x.

[38] S. Chang, Y. Hu, J. Qian, Y. Shao, S. Ni, L. Kong, W. Dan, C. Luo, S. Jin, X. Xu, Mg2TiO4 spinel modified by nitrogen doping as a visible-light-active photocatalyst for antibacterial activity, Chem. Eng. J. 410 (2021), 128410, https://doi.org/10.1016/j.cej.2021.128410.

[39] T.D. Boyko, C.E. Zvoriste, I. Kinski, R. Riedel, S. Hering, H. Huppertz, A. Moewes, Anion ordering in spinel-type gallium oxonitride, Phys. Rev. B 84 (2011), 085203, https://doi.org/10.1103/PhysRevB.84.085203.

[40] P.A. Tempest, R.K. Wild, Thickness measurements of spinel and chromia layers in stainless steel oxide scales by X-ray diffractometry, Oxid. Metals 17 (1982) 345–357, https://doi.org/10.1007/BF00742116.

[41] S. Tuzi, K. Göransson, S.M.H. Rahman, S.G. Eriksson, F. Liu, M. Thuvander, K. Stiller, Oxide evolution on Alloy X-750 in simulated BWR environment, J. Nucl. Mater. 482 (2016) 19–27, https://doi.org/10.1016/j.jnucmat.2016.09.026.

[42] N. Itagaki, K. Kakiuchi, Y. Mozumi, T. Furuya, O. Kubota, Development of new high corrosion resistance Zr Alloy HiFi for high burn-up BWR fuel, Proc. Eur. Nucl. Soc. TOPFUEL (2003).

[43] A. Inspektor, P.A. Salvador, Architecture of PVD coatings for metalcutting applications: a review, Surf. Coat. Technol. 257 (2014) 138–153, https://doi.org/10.1016/J.SURFCOAT.2014.08.068.

[44] A. Baptista, F.J.G. Silva, J. Porteiro, J.L. Míguez, G. Pinto, L. Fernandes, On the physical vapour deposition (PVD): evolution of magnetron sputtering processes for industrial applications, Procedia Manuf. 17 (2018) 746–757, https://doi.org/10.1016/j.promfg.2018.10.125.

[45] D.V. Sidelev, S.E. Ruchkin, M.S. Syrtanov, E.B. Kashkarov, I.A. Shelepov, A.G. Malgin, K.K. Polunin, K.V. Stoykov, A.A. Mokrushin, Protective Cr coatings with CrN/Cr multilayers for zirconium fuel claddings, Surf. Coat. Technol. 433 (2022), https://doi.org/10.1016/J.SURFCOAT.2022.128131.

[46] J. Krejčí, J. Kabátová, F. Manoch, J. Kočí, L. Cvrček, J. Málek, S. Krum, P. Šutta, P. Bublíková, P. Halodová, H.K. Namburi, M. Ševeček, Development and testing of multicomponent fuel cladding with enhanced accidental performance, Nucl. Eng. Technol. 52 (2020) 597–609, https://doi.org/10.1016/J.NET.2019.08.015.

[47] A. Fazi, K. Stiller, H.-O. Andrén, M. Thuvander, Cold sprayed Cr-coating on Optimized ZIRLO™ claddings: the Cr/Zr interface and its microstructural and chemical evolution after autoclave corrosion testing, J. Nucl. Mater. 560 (2022), 153505, https://doi.org/10.1016/j.jnucmat.2022.153505.

[48] A. Fazi, M. Sattari, T. Boll, M. Strach, K. Stiller, H.-O. Andrén, D. Adorno Lopes, M. Thuvander, Atom probe data used in "CrN–NbN nanolayered coatings for enhanced accident tolerant fuels in BWR," (2023). https://doi.org/https://doi.org/10.6084/m9.figshare.23257427.